Surface-emitting mid-infrared quantum cascade lasers with high-contrast photonic crystal resonators

Gangyi Xu[1,3], Raffaele Colombelli[1,4], Remy Braive[2], Gregoire Beaudoin[2], Luc Le Gratiet[2], Anne Talneau[2], Laurence Ferlazzo[2], and Isabelle Sagnes[2]

[1]*Institut d'Electronique Fondamentale, Université Paris-Sud and CNRS, UMR8622, 91405 Orsay, France*
[2]*Laboratoire de Photonique et Nanostructures, LPN/CNRS, Route de Nozay, 91460 Marcoussis, France*
[3]*gangyi.xu@u-psud.fr*
[4]*raffaele.colombelli@u-psud.fr*

Abstract: We have developed surface-emitting single-mode quantum cascade lasers which employ high-contrast photonic-crystal resonators. The devices operate on band-edge states of the photonic band-structure. The mode profile and polarization characteristics of the band-edge modes are calculated by three-dimensional finite-difference time-domain simulation. Experimentally, the spectral properties, the far-field patterns, and the polarization characteristics of the lasers are determined and compared with simulations. The good agreement between the simulations and the experiments confirms that the hexapolar mode at the Γ-point band-edge gives rise to lasing. By using a novel and advanced fabrication method, deep and vertical PhC holes are fabricated with no metal redeposition on the sidewalls, which improves the laser performance with respect to the current status. The angular of the output beam is $\approx 15^{\circ}$, and the side mode suppression ratio of the single mode emission is about 25 dB. The threshold current density at 78K and the maximum operation temperature are 7.6 kA/cm^2 and 220 K, respectively. The performance is mainly limited by the loss induced by surface plasmon waveguide, which can be overcome by using an optimized dielectric waveguide structure.

OCIS codes: (140.5960) Semiconductor lasers; (230.5750) Resonators; (240.6680) Surface plasmons.

References and links

1. R. Colombelli, K. Srinivasan, M. Troccoli, O. Painter, C. Gmachl, F. Capasso, D. M. Tennant, A. M. Sergent, D. L. Sivco, , and A. Y. Cho, "Quantum Cascade Photonic-Crystal Surface-Emitting Laser," Science **302**, 1374 (2003).
2. K. Srinivasan, O. Painter, R. Colombelli, C. Gmachl, D. M. Tennant, A. M. Sergent, D. L. Sivco, A. Y. Cho, M. Troccoli, and C. F, "Lasing mode pattern of a quantum cascade photonic crystal surface-emitting microcavity laser," Appl. Phys. Lett. **84**, 4164–4166 (2004).
3. Hua Zhang, L. Andrea Dunbar, Giacomo Scalari, Romuald Houdr, and Jrme Faist, "Terahertz photonic crystal quantum cascade lasers," Opt. Express 15, 16818-16827 (2007)
4. A. Benz, C. Deutsch, G. Fasching, K. Unterrainer, A. Andrews, P. Klang, W. Schrenk, and G. Strasser, "Active photonic crystal terahertz laser," Opt. Express **17**, 941–946 (2009).

#126141 - $15.00 USD Received 29 Mar 2010; revised 3 May 2010; accepted 3 May 2010; published 21 May 2010

5. Y. Chassagneux, R. Colombelli, W. Maineult, S. Barbieri, H. E. Beere, D. A. Ritchie, S. P. Khanna, E. H. Linfield, and G. A. Davies, "Electrically pumped photonic crystal terahertz lasers controlled by boundary conditions," Nature **457**, 174 (2009).
6. G. Xu, V. Moreau, Y. Chassagneux, A. Bousseksou, R. Colombelli, G. Patriarche, G. Beaudoin, and I. Sagnes, "Surface emitting quantum cascade lasers with metallic photonic-crystal resonators," Appl. Phys. Lett. **94**, 221101 (2009).
7. Y. Chassagneux, R. Colombelli, W. Maineult, S. Barbieri, S. Khanna, E. Linfield, and A. Davies, "Graded photonic crystal THz quantum cascade lasers," Appl. Phys. Lett. **96**, 031104 (2010).
8. Y. Chassagneux, R. Colombelli, W. Maineult, S. Barbieri, S. Khanna, E. Linfield, and A. Davies, "Predictable surface emission patterns in terahertz photonic-crystal quantum cascade lasers," Opt. Express **17**, 9491–9052 (2009).
9. G. Xu, Y. Chassagneux, R. Colombelli, G. Beaudoin, and I. Sagnes, "Polarized single-lobed surface emission in mid-infrared, photonic-crystal, quantum-cascade lasers," Opt. Lett. **35**, 859 (2010).
10. K. Unterrainer, R. Colombelli, C. Gmachl, F. Capasso, H. Y. Hwang, A. M. Sergent, D. L. Sivco, and A. Y. Cho, "Quantum cascade lasers with double metal-semiconductor waveguide resonators," Appl. Phys. Lett. **80**(17), 3060–3062 (2002).
11. S. Kohen, B. Williams, and Q. Hu, "Electromagnetic modeling of terahertz quantum cascade laser waveguides and resonators," J. Appl. Phys. **97**, 053106 (2005).
12. O. Painter, R. Lee, A. Scherer, A. Yariv, J. O'Brien, P. Dapkus, and I. Kim, "Two-dimensional photonic band-gap defect mode laser," Science **284**, 1819-1821 (1999).
13. M. Bahriz, V. Moreau, J. Palomo, R. Colombelli, D. Austin, J. Cockburn, L. Wilson, A. Krysa, and J. Roberts, "Room-temperature operation of $\lambda = 7.5$ μm surface-plasmon quantum cascade lasers," Appl. Phys. Lett. **88**, 181103 (2006).
14. B. D'Urso, O. Painter, J. O'Brien, T. Tombrello, A. Scherer, and A. Yariv, "Modal reflectivity in finite-depth two-dimensional photonic-crystal microcavitites," J. Opt. Soc. Am. B **15**(3), 1155–1159 (1998).
15. The finite elements solver Comsol Multiphysics has been employed for the simulations. Bloch-periodic boundary conditions where implemented .
16. M. Imada, A. Chutinan, S. Noda, and M. Mochizuki, "Multidirectionally distributed feedback photonic crystal lasers," Phys. Rev. B **65**(19), 195306 (2002).
17. A. Bousseksou, V. Moreau, R. Colombelli, C. Sirtori, G. Patriarche, O. Mauguin, L. Largeau, G. Beaudoin, and I. Sagnes, "Surface-plasmon distributed-feedback mid-infrared quantum cascade lasers based on hybrid plasmon/air-guided modes," IEEE Electron. Lett. **44**, 807 (2008).
18. K.-H. Lee, S. Guilet, G. Patriarche, I. Sagnes, and A. Talneau, "Smooth sidewall in InP-based photonic crystal membrane etched by N2-based inductive coupled plasma," J. Vac. S. Tech. B **26**, 1326–1333 (2008).
19. G. Vecchi, F. Raineri, I. Sagnes, A. Yacomotti, P. Monnier, T. Karle, K.-H. Lee, R. Braive, L. L. Gratiet, S. Guilet, G. Beaudoin, A. Talneau, S. Bouchoule, A. Levenson, and R. Raj, "Continuous-wave operation of photonic band-edge laser near 1.55 m on silicon wafer," Opt. Express **15**, 7551–7556 (2008).
20. A. Farjadpour, D. Roundy, A. Rodriguez, M. Ibanescu, P. Bermel, J. D. Joannopoulos, S. G. Johnson, and G. Burr, "Improving accuracy by subpixel smoothing in FDTD," Opt. Lett. **31**, 2972–2974 (2006).
21. S. G. Johnson, S. Fan, P. R. Villeneuve, J. D. Joannopoulos, and L. A. Kolodziejaki, "Guided modes in photonic crystal slabs," Phys. Rev. B **60**(8), 5751–5758 (1999).
22. S. H. Kim, S. K. Kim, and Y. H. Lee, "Vertical beaming of a wavelength-scale photonic crystal resonator," Phys. Rev. B **73**, 235117 (2006).
23. J. Vučković, M. Loncar, H. Mabuchi, and A. Scherer, "Optimization of the Q factor in photonic crystal Microcavities," IEEE J. Quantum Electron. **38**, 850 (2002).
24. H. Y. Ryu, M. Notomi, and Y. H. Lee, "Finite-difference time-domain investigation of band-edge resonant modes in finite-size two-dimensional photonic crystal slab," Phys. Rev. B **68**, 045209 (2003).
25. L. Sapienza, A. Vasanelli, R. Colombelli, C. Ciuti, Y. Chassagneux, C. Manquest, U. Genner, and C. Sirtori, "Electrically Injected Cavity Polaritons," Phys. Rev. Lett. **100**, 136806 (2008).
26. A. Bousseksou, R. Colombelli, A. Babuty, Y. De Wilde, Y. Chassagneux, C. Sirtori, G. Patriarche, G. Beaudoin, and I. Sagnes, "A semiconductor laser device for the generation of surface-plasmons upon electrical injection," Opt. Express **17**, 9391 (2009).

1. Introduction

Photonic-crystal (PhC) quantum cascade (QC) lasers merge photonic and electronic band structure engineering. In particular, the use of a PhC resonator yields surface-emission - with possibly reduced divergence - and simultaneously spectrally single-mode behavior. Both these characteristics can be of interest for fundamental and application-driven reasons [1–9]. To date, PhC QC lasers have been demonstrated both in the mid-infrared and in the THz spectral ranges, but

#126141 - $15.00 USD Received 29 Mar 2010; revised 3 May 2010; accepted 3 May 2010; published 21 May 2010

only in the so-called band-edge configuration where the device operates on band-edge states of the photonic band structure [1, 5–9]. These states - typically located at high-symmetry points in the band structure - exhibit a high photonic density of states (and correspondingly reduced group velocity) as a result of the two-dimensional distributed feedback of the photonic lattice.

Various implementations for PhC QC lasers have been proposed. The first surface-emitting PhC QC laser was demonstrated by Colombelli et al. in the mid-IR [1]. Deep and vertical air holes were ICP (inductively coupled plasma) etched into the semiconductor laser layers in order to obtain the necessary index contrast (3.4 *vs* 1 in this case), and reduce the device dimensions. A similar approach was employed in the THz by Zhang et al. [3] and Benz et al. [4], where a photonic structure made of deep etched micro-pillars provides at the same time gain and in-plane optical confinement. In both cases the vertical mode confinement relied on metal-metal waveguides [10, 11], and the lasers operate in an edge-emitting configuration. Recently however, we have demonstrated a novel approach: a metallic photonic crystal, consisting of air holes in a thin metallic layer, is directly written on the top device metallization and no semiconductor etch is needed [5, 6]. The operation of the PhC in this case can be understood in an intuitive way: the electromagnetic field distributions of the guided mode when the top metallization is present or absent are very different. This large modal mismatch plays the same role as the index contrast in standard PhCs, thus giving rise to optical feedback and eventually to lasing. This method has been used successfully in both the THz and mid-infrared spectral ranges [6, 8]. Most importantly, judicious design of the PhC resonator permits to precisely engineer the far-field emission pattern, the divergence angle and the polarization characteristics of the laser [7, 9].

In order to fabricate more compact PhC QC lasers, or even PhC devices which operate on a defect mode [12], achieving an elevated index contrast is crucial. This is particularly true in the mid-IR, where the sole patterning of the metal - though efficient - cannot induce a high index contrast. In this work, we improve the method originally employed by Colombelli et al. [1]. A strategy for PhC fabrication is proposed which improves both the device yield and the laser performance with respect to Ref. [1]. Besides obtaining surface laser emission with a very low divergence angle, we provide a systematic experimental and theoretical study of the device photonic band structure, as well as their far-field and polarization characteristics. Excellent agreement is obtained between theory and experiment.

The paper is organized as follows. In Sec. II the design of the PhC-QCLs is described: the photonic-band structure and the electromagnetic field distribution of the band-edge modes are presented. Section III focuses on material growth and device fabrication. Section IV contains the experimentally measured spectral properties below threshold. Section V discusses the device characteristics in the lasing-regime, including the light-current-voltage features, temperature behavior, the far-field patterns, and the polarization characteristics. In Sec. VI, three-dimensional (3D) finite-difference time-domain (FDTD) simulations are performed which provide the lasing mode identification. Section VII contains the conclusion.

2. Design

Figure 1(a) shows the schematic structure of a typical PhC-QCL studied in this work. A surface-plasmon waveguide is employed for vertical confinement [13], i.e. the QC laser active region is sandwiched between an InP substrate and directly top metallization layers, instead of top dielectric claddings. The top metallic film acts simultaneously as surface plasmon carrying layer, and as contact layer for electric current injection. The air holes which constitute the triangular PhC lattice are ICP etched through the semiconductor active region and deep into the substrate. Although the surface plasmon waveguide will induce relatively large ohmic losses in the mid-IR range, it is crucial for the operation of our PhC device. In a surface plasmon waveguide struc-

#126141 - $15.00 USD Received 29 Mar 2010; revised 3 May 2010; accepted 3 May 2010; published 21 May 2010

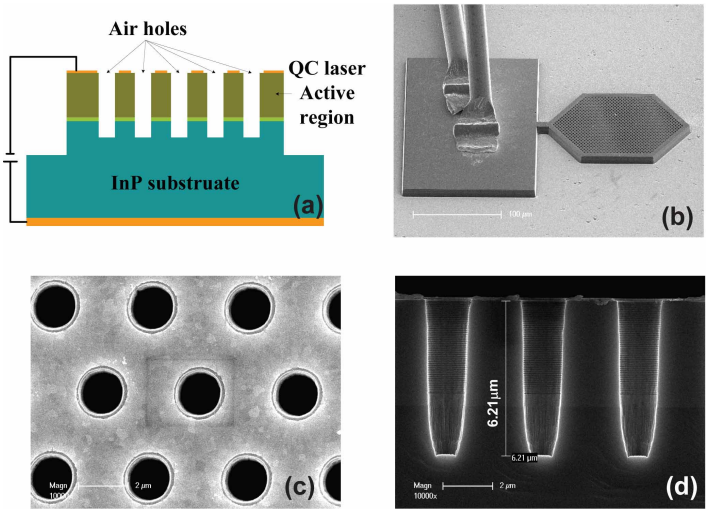

Fig. 1. (a) Schematic cross section of a PhC device. (b) Scanning electron microscope (SEM) image of a typical device. The SEM top view and cross-section of the central part of the PhC structure are shown in panels (c) and (d), respectively. In particular, panel (c) shows the extremey precise alignment between first and second level ebeam lithography.

ture, the electromagnetic (EM) field is bound at the interface between the top metallic layer and the active region, and it decays approximately exponentially into active region. This feature, allows one to confine most of the EM field in the PhC structure, and to reduce the unwanted radiation diffraction into the substrate, with a reasonably deep semiconductor etch [14]. The photonic band structures in the following are calculated by solving the 3D Helmholtz equation with Bloch periodic boundary conditions [15]. Figure 2(a) reports the photonic band structure of a real laser, in which the lattice period is $a = 3.6\ \mu m$, the radius of the air holes is $r/a = 0.24$, and the etching depth is 6.2 μm. The band diagram is presented in wavenumbers, and also in relative frequency units a/λ. The calculations target the nominal QC laser emission wavelengths $\approx 9.5\ \mu m$. The band-edge states modes in the light cone - highlighted with light gray regions - are of special interest in Fig. 2(a). Their flat dispersion yields an enhanced photonic density of states, which makes them good candidates for lasing. The six band edge states can be divided into 3 groups at different frequencies [16] [groups A, B and C in Fig. 2(a)]. Group A consists of three band-edge modes at Γ-point: one hexapolar mode (with reduced frequency $a/\lambda = 0.355$), and two degenerated quadrupole modes ($a/\lambda = 0.359$). Group B consists of a quadrupole mode at $k_x = 0$, $k_y \approx \pi/(3a)$, and the reduced frequency is $a/\lambda = 0.372$. Group C consists of two degenerated dipole mode ($a/\lambda = 0.388$) at Γ point. The distributions of the electric field component orthogonal to the semiconductor layers (E_z) for the six band-edge states are given in Fig. 3. The profile and the symmetry characteristics of the band-edge states determine the emission far-field pattern symmetry and the polarization, from which the lasing mode can be identified.

For these 6 band-edge modes, Table 1 shows the normalized frequency, the waveguide loss and the confinement factors over the active laser region. Since the modes are calculated in the approximation of infinite structure with Bloch-periodic boundary conditions, the loss listed in Table 1 only represents the waveguide loss and does not include the finite-size resonator loss, which will be calculated by 3D FDTD simulations in Sec. 6. Table 1 indicates that the hexapolar mode is the most probable candidate for lasing for its low waveguide loss and high confinement

#126141 - $15.00 USD Received 29 Mar 2010; revised 3 May 2010; accepted 3 May 2010; published 21 May 2010

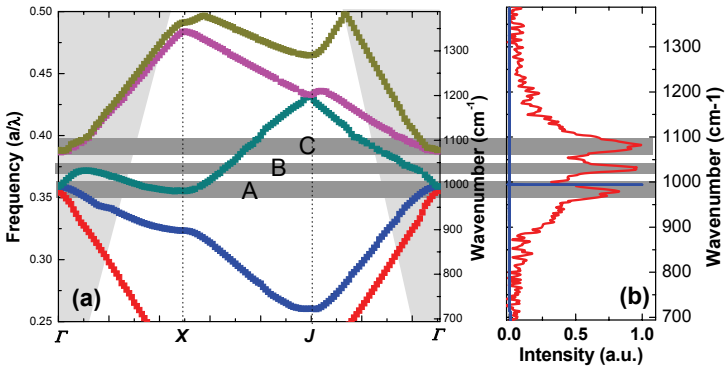

Fig. 2. (a) Calculated photonic band structure of the PhC. The y-axis in absolute frequency units refers to a structure with active region thickness 3.5 μm, etching depth 6.2 μm, lattice period $a = 3.6$ μm, radius of the air holes $r/a = 0.24$. The light gray regions correspond to the light cone. The dark gray horizontal bands highlight the three groups of band-edge modes relevant for lasing. (b) EL spectrum (red curve) measured under threshold at a temperature of 300K. The blue curve is the lasing spectrum of the same device, measured above threshold and at the maximum operation temperature (220K). The intensity is normalized. The absolute frequency scales are identical since the laser structure parameters are the same as those used in the calculation of the photonic band structure.

Table 1. Normalized frequency, waveguide loss and confinement factors of the band-edge modes calculated for an infinite PhC structure. All the modes except the one marked by "*" are at the Γ point of the photonic-band structure. The mode marked by "*" is at $k_x = 0$, $k_y = \pi/(3a)$.

Mode	Normalized frequency (a/λ)	Waveguide loss (cm^{-1})	Confinement factor
Hexapole	0.355	28.8	0.96
Quadrupole	0.359	33.6	0.93
Quadrupole	0.359	33.2	0.93
Quadrupole*	0.372	42.0	0.91
Dipole	0.388	52.2	0.80
Dipole	0.388	55.2	0.80

factor. However, the difference in waveguide loss and confinement factor between the hexapolar and the two quadrupolar modes at the Γ-point are small. As a consequence, in order to identify the lasing mode, it is necessary to take into account the cavity loss and compare the calculated far-field pattern and polarization characteristics of different modes with the measured results.

#126141 - $15.00 USD Received 29 Mar 2010; revised 3 May 2010; accepted 3 May 2010; published 21 May 2010

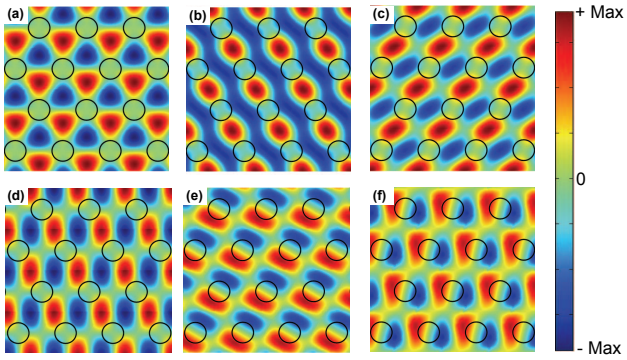

Fig. 3. Electric field distribution (E_z) of the six band-edge modes in proximity of the Γ-point of the photonic band structure. The calculation is performed for an infinite periodic lattice. The distribution of E_z is a section parallel to the semiconductor layers, which has been taken at the middle of active region. (a) shows the hexapolar mode at Γ-point ($a/\lambda = 0.355$). (b) and (c) show the two degenerated quadrupolar modes at the Γ-point ($a/\lambda = 0.359$), (d) shows the quadrupolar mode at $k_x = 0$, $k_y \approx \pi/(3a)$, with reduced frequency $a/\lambda = 0.372$. (e) and (f) show the two degenerated dipolar modes at Γ-point ($a/\lambda = 0.388$).

3. Semiconductor growth and device fabrication

The QC laser heterostructure (sample InP857) was grown by metal organic vapor phase epitaxy (MOVPE) in a VEECO-D-180 turbo disk MOVPE chamber, using an $In_{0.53}Ga_{0.47}As/Al_{0.48}In_{0.52}As$ lattice matched to a highly n-doped (001) InP substrate ($n \approx 10^{18}$ cm^{-3}). The active region is based on a three-phonon-resonance design, with nominal lasing transition at $\lambda = 9.5$ μm. Forty active-region/injector stages were grown, preceded by a 2-μm-thick low-doped InP ($n = 5 \times 10^{16}$ cm^{-3}) buffer layer and 500-nm-thick InGaAs ($n = 1 \times 10^{17}$ cm^{-3}), and followed by thin 100-nm-thick InGaAs contact facilitating layers. The details of the typical material growth procedure - for a slightly different emission wavelength - are given in Ref. [17].

The main fabrication challenges for mid-IR PhC QC lasers are (i) to achieve a deep and simultaneously vertical etch of the air holes and (ii) to deposit the top metallization layer on the semiconductor part only, and not inside the holes (see Fig. 1). In previous work [1], the top metallization layer was deposited on the whole device surface after the PhC etch. As a result, the sidewalls and the bottom of the air holes were metal-covered, which unavoidably induced large optical losses, and reduced device yield.

In this work, an advanced fabrication method is developed which overcomes the problems mentioned above. Two extremely carefully aligned e-beam lithography steps are used for each device. A 100 keV LEICA electron-beam writer with 5 nm resolution was used. The two mask levels are identical, except for the air holes radius which in the 1st mask is 100 nm larger than in the 2^{nd} mask. The first ebeam mask is used to define the top metallic layer: a triangular lattice of air holes obtained by lift-off in a thin (100 nm) Au metallization. The second level is used to define the SiN hard-mask for semiconductor ICP etching. Since the air holes in the second level are slightly smaller, the metallic layer will not be attacked nor damaged by the plasma etch. Note: thanks to the extremely precise alignment between the two mask levels, the radius difference between the metallic PhC holes and the semiconductor air holes can be kept much below the emission wavelength [$\approx$ 100nm, see Figs. 1(c) and 1(d)]. The light behavior in the PhC resonator will therefore not be affected.

The process starts with the fabrication of etched alignment marks, followed by SiN PECVD-

#126141 - $15.00 USD Received 29 Mar 2010; revised 3 May 2010; accepted 3 May 2010; published 21 May 2010

deposition (200 nm) for electric current isolation. The passivation layer is then opened by reactive-ion-etching (RIE) at the PhC device sites. After realization of the contact pads (lift-off of 30nm/300nm Ti/Au), the metallic PhC is defined by e-beam lithography followed by lift-off of a 100-nm-thick Au layer. A 1.5-μ m-thick SiN layer was then deposited: it acts as the hard mask layer for the semiconductor ICP etch. The second PhC pattern is then aligned and generated by e-beam lithography, transferred into the SiN layer by RIE, and finally transferred into the semiconductor layers by ICP etch up to a depth of 6.2 μm [Figs. 1(b) and 1(d)] [18]. The SiN hard mask is finally removed and back-contact deposition (Ti/Au) concludes the process.

A series of PhC-QC lasers were fabricated, with photonic lattice periods in the $3.0-to-3.8\mu$m range and r/a value fixed at 0.24 [Fig. 1(c)]. The dimension of the PhC structure, defined as the diameter of a circle circumscribing the hexagonal PhC device, is 150 μm. Figure 1(b) shows the scanning electron microscope image of a typical device; its central part is presented in Fig. 1(c). Figure 1(d) shows the cross-section of the PhC structure, demonstrating deep and vertical air holes.

4. Spectral properties below laser threshold

Electroluminescence (EL) spectra taken from the surface of the fabricated PhC-QC lasers were measured in pulsed mode, up to a temperature of 300K starting from 78K. Some of the results at 78K are given in Fig. 4(a) for devices with different lattice spacings. The EL spectrum measured in the same conditions from a standard Fabry-Prot laser fabricated with the same material is also shown for reference. The PhC QC lasers exhibit three relatively narrow and clearly identifiable resonances, which emerge from the wide emission background corresponding to the active region bare EL. Their peak wavelength tunes linearly with the lattice period, as shown in Fig. 4(b), thus proving that they originate from resonant oscillations in the PhC resonator.

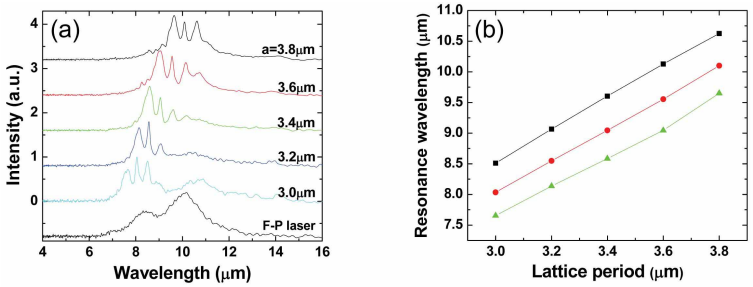

Fig. 4. (a) EL spectra of devices with the same $r/a = 0.24$, but with different photonic lattice periods. The EL spectrum of a Fabry-Perot ridge laser fabricated with the same material is also shown. The spectra are measured at 78K in pulsed mode. The pulse width is 5 μs, the repetition frequency is 84 kHz, and the current density is 0.6 kA/cm^2. (b) Peak emission wavelength of the PhC resonances of panel (a) plotted as a function of the photonic lattice period. The dependence is correctly linear.

We can precisely assign each emission peak to a specific band edge, by comparing the EL spectrum with the photonic band structure. Figure 2(b) (red curve) shows the EL spectrum of a device with the same PhC structure as the one used in the calculation of the photonic band-structure of panel (a). The EL spectrum is collected at 300K with a LN-cooled HgCdTe detector, using lock-in technique and a FTIR spectrometer operated in step scan mode. The clear resonance, observed in the EL spectrum *even at room temperature*, demonstrates that strong optical feedback is achieved by using a deep-etched PhC structure. Furthermore, the frequency ranges corresponding to the observed resonances are in excellent agreement with the

#126141 - $15.00 USD Received 29 Mar 2010; revised 3 May 2010; accepted 3 May 2010; published 21 May 2010

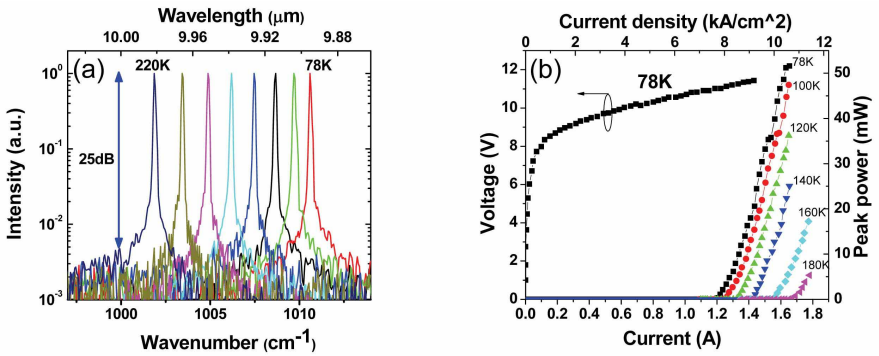

Fig. 5. Lasing spectra (a) and light-current-voltage characteristics (b) of a typical device measured in pulsed mode at different heat sink temperatures. The pulse width is 50ns, and the repetition frequency is 84 kHz. The maximum operating temperature is 220K. For comparison, the T_{max} of Fabry-Perot lasers with the same active material is 240K.

three groups of band-edge modes with high optical density of states which we had identified (monopolar, bipolar, quadrupolar and hexapolar). We can therefore confirm that the observed emission resonances find their origin in the delocalized band-edge modes in the photonic crystal resonator.

5. Laser regime: light-current-voltage characteristics, temperature behavior, far-field emission patter and polarization

Upon higher current injection, the devices achieve lasing, with emission from the top surface. Figure 5(a) shows the spectra of a typical device measured in pulsed mode at different heat-sink temperatures. Single mode emission with a side-mode suppression ratio (SMSR) of at least 25 dB is observed. Note: the emission is single mode for all injected currents and operation temperatures explored, with a maximum operation temperature (T_{max}) of 220K. The light-current-voltage (L-I-V) characteristics of the device at different temperatures are reported in Fig. 5(b). The threshold current density (J_{th}) at 78K is 7.6 kA/cm^2, and it increases to 10.8 kA/cm^2 at 180K. The peak output power reaches 52 mW at 78 K, and decreases to 6 mW at 180K. The device performance - in terms of J_{th} - is comparable, if a little degraded, to standard FP lasers (J_{th}=5.6 kA/cm^2 at 78K) fabricated with the same material, which operated up to a T_{max} of 240K.

We characterized the far field surface emission patterns and the polarization characteristics of the lasers by scanning a LN-cooled HgCdTe detector on a 15-cm-radius sphere centered on the device. The results for a typical device are reported in Fig. 6(a), where the $\theta_x = \theta_y = 0$ angle corresponds to the direction orthogonal to the device surface. The far-field patterns have a "doughnut" shape, a typical feature of PhC lasers operating on band-edge states [19]. The surface-emission divergence is $\approx 15^\circ$, demonstrating an almost diffraction-limited angular spreading. Figures 6(b) and 6(c) show the two orthogonally polarized far-field emission patterns (the polarization direction is indicated by the white arrows). For these measurements, a metallic grating polarizer is placed directly in front of the LN-cooled HgCdTe detector. The far-field pattern polarized along the θ_y direction [Fig. 6(b)] has four lobes which are mirror symmetric with respect to the θ_x- and θ_y-axis. In particular, the $\theta_x = \theta_y$ and $\theta_x = -\theta_y$ directions are nodal lines, and no emission intensity is detected. The far-field polarized along the θ_x direction [Fig. 6(c)] presents 4 lobes too, but the nodal lines are rotated by 45° , corresponding to the $\theta_x = 0$ and $\theta_y = 0$ directions. Furthermore, the intensity is 50% less intense in this polarization.

#126141 - $15.00 USD Received 29 Mar 2010; revised 3 May 2010; accepted 3 May 2010; published 21 May 2010

6. 3D FDTD simulation: lasing mode identification

In order to perform the FDTD simulations, it is useful to identify the symmetry of the lasing mode. In Fig. 2(b) the lasing spectrum has been added besides the EL spectra of the same device (blue curve). The lasing frequency corresponds to the A-labeled resonance. A comparison with the calculated photonic band structure allows one to infer that the laser should operate on the quadrupolar or on the hexapolar modes. Our working hypothesis is that the device operates on the latter one. 3D FDTD simulations were performed in order to calculate the quality (Q) factor, and the electromagnetic field distribution of the band-edge mode responsible for lasing [20–22]. The far-field pattern is also calculated with a standard near-to-far-field transform with a Fourier-transform approach [23, 24].

Figure 7 shows the schematic horizontal view and cross-section of the numerical simulation domain. In order to reduce the computational time, the calculation was performed for only an 8-period photonic crystal instead of the 21 periods of the real devices. Perfectly matched layer (PML) boundary conditions are employed, and - for simplicity - the metallic layers are approximated as perfect metals. Furthermore, only the real parts of the index of refraction are used for the InGaAs/AlInAs active region ($n = 3.25$) and the InP substrate ($n = 2.9$). The other

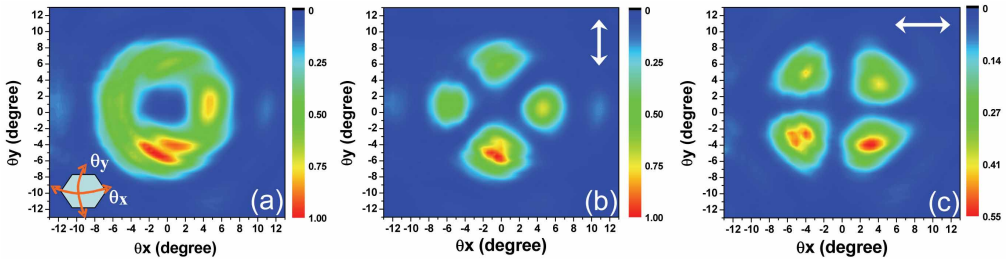

Fig. 6. (a) Far-field measured at 78K in pulsed mode (50ns at 84 kHz). (b) and (c) far-field patterns measured with a linear polarizer placed in front of the detector in the $\theta_y$and θ_x directions, respectively. The arrows show the polarization direction, and the inset of panel (a) defines the scan directions. The angular resolution is 0.5 degrees. The sample-to-detector distance is 15 cm.

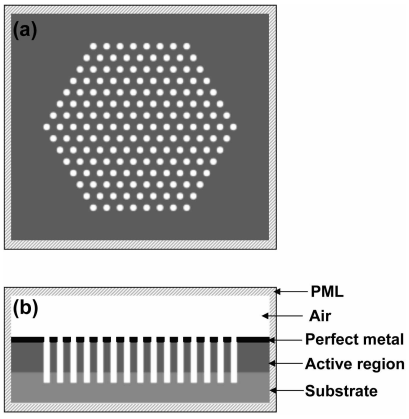

Fig. 7. Horizontal view (a) and cross-section (b) of the FDTD calculation domain surrounded by perfectly matched layer boundaries. The number of periods of the simulated PhC resonator, starting from the center, is 8. The top metallization layer is approximated as perfect metal. The index of the active region and substrate are 3.25 and 2.9, respectively.

#126141 - $15.00 USD Received 29 Mar 2010; revised 3 May 2010; accepted 3 May 2010; published 21 May 2010

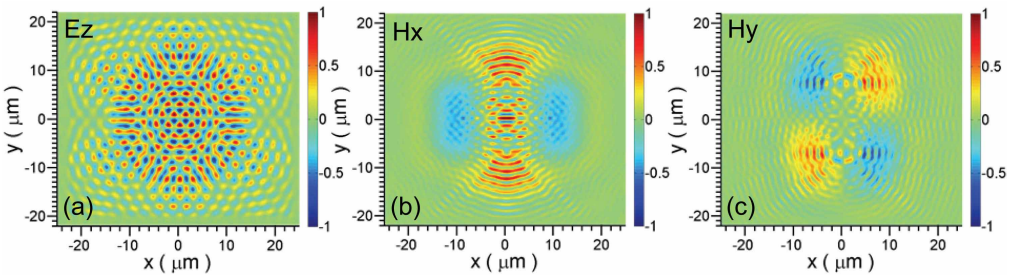

Fig. 8. (a) Distribution of the electric field (E_z) in the PhC plane taken in the middle of the active region. The calculation is the result of the 3D FDTD simulation. (b) and (c) show the x (H_x) and y (H_y) components of the transverse magnetic fields in the near-field, which is 5 μm above the PhC surface.

parameters of the PhC structure, including the lattice period, the radius and the etching depth of the air holes, are the same as in the real device.

We first compared the calculated total *Q*-factors of the three candidate modes for lasing. The hexapolar mode *Q*-factor is 230, contrary to the two quadrupole modes whose *Q*-factors are very low (one is 80, and the other one is lower than 50 which is the threshold value set in the simulation). The numerical results indicate that the device is most probably operating on the hexapolar mode.

The electromagnetic field distribution of the hexapolar mode is reported in Fig. 8. Panel (a) shows the electric field (E_z component) across a section - in the plane of the PhC resonator - located in the middle of the active region. Note that in the central region of the resonator, the profile and symmetry of E_z are identical to the case of an infinite PhC, as in Fig. 3. However, the EM field profile is gradually deformed when moving from the center to the edge of the resonator. This effect is crucial: it is in fact the finite size of the resonator which allows the hexapolar mode to be radiative. In an infinite PhC in fact, the hexapolar mode would not couple to freely propagating photons. Figures 8(b) and 8(c) show - respectively - the x (H_x) and y (H_y) components of the transverse magnetic field in the device near-field, 5 μm above the surface of the PhC. The H_x and H_y components are necessary to deduce the far-field emission pattern.

Figure 9(a) shows the calculated time-averaged intensity of the electric field ($|E_{y,far}|^2$ + $|E_{x,far}|^2$) in the far field, obtained from the H_x and H_y magnetic field components using the procedure described in Refs. [8, 23, 24]. Figures 9(b) and 9(c) report instead the calculated intensity of the electric field $|E_{y,far}|^2$ and $|E_{x,far}|^2$ in the far field. They correspond to the measured far-field patterns polarized in the θ_y and θ_x directions, and they are in qualitative good agreement with the measurements reported in Fig. 6. Even the weak features in the measurements are well reproduced by the simulation. However, the measured divergence angle (15°) is much narrower than the simulated one (50°). The reason is that the far-field simulation has been run on a smaller PhC resonator than the real device (8 periods instead of 21).

These findings positively identify the lasing mode and demonstrate that the device is indeed operating on an hexapolar band-edge. Note also that purely metallic PhC lasers, as in Ref. [6], tend instead to lase on monopolar states since these latter ones reduce the EM overlap with the metal and therefore lead to reduced losses.

7. Conclusions

We have developed an advanced fabrication method for high-index-contrast PhC QC lasers. The high-index-contrast is obtained by etching deep holes in the semiconductor layers. The

#126141 - $15.00 USD Received 29 Mar 2010; revised 3 May 2010; accepted 3 May 2010; published 21 May 2010

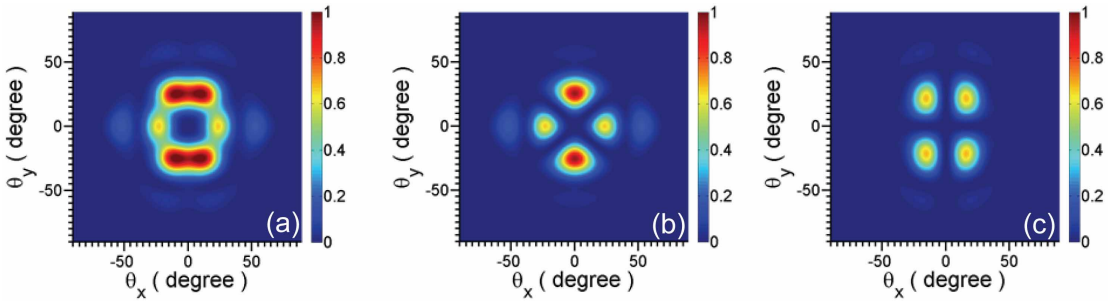

Fig. 9. (a) Calculated far-field pattern. (b) and (c) show the component of the far-field pattern polarized in θ_y and θ_x directions, respectively. The symmetry and polarization are in excellent agreement with the experimental results in Fig. 6. However, the angular divergence is larger than in the experiment, since the simulated PhC - for computational reasons - has only 8 periods instead of 21.

new fabrication strategy allows one to improve both the device yield and the device performance with respect to Ref. [1], where PhC QC lasers were originally developed. In particular, the device EL shows narrow PhC resonances up to room temperature. These PhC resonators are therefore ideally suited to be be applied to the study of intersubband polaritons [25]. We have experimentally systematically studied the device spectral properties below and above laser threshold, their far-field emission patterns, and polarization characteristics. The comparison with 3D FDTD simulations shows good agreement between theory and experiment, and allows the identification of the lasing mode. More importantly, we have now developed a full understanding of this system, and the use of 3D simulations will possibly allow the improvement of the extraction efficiency in surface-emitting PhC QC lasers.

The spectral and spatial properties of the devices are very good: the angular divergence of the output beam is close to the diffraction-limit, and the SMSR of the the single mode emission is at least 25dB. However, the temperature performance of the device is not satisfactory and needs to be improved. Here, the main performance limitation is constituted by the surface plasmon waveguide (it introduces large ohmic losses, of the order of 30/40 cm^{-1}), which was originally employed to avoid excessive radiation diffraction in the substrate [1, 14]. One possible strategy towards performance improvement is to develop techniques to reduce the plasmonic losses *via* metal patterning, similarly to what was achieved in Ref. [26] in the case of metallic 1^{st} order DFB lasers. A second possibility is to develop dielectric waveguide structures with reduced thickness - for compatibility with the PhC approach - and simultaneously low loss.

Acknowledgements

We thank S. Bouchoule for discussions and help with the ICP etching development, and X. Checoury for useful discussions. This work was conducted as part of a EURYI scheme award (www.esf.org/euryi), and was also partially supported by the French National Research Agency (ANR MetalGuide).

#126141 - $15.00 USD Received 29 Mar 2010; revised 3 May 2010; accepted 3 May 2010; published 21 May 2010